Scientific Reports

https://doi.org/10.1038/s41598-026-43520-w

Article in Press

Application of UAV photogrammetry technology in identifying discontinuities in slopes in the Pulang copper mine

Received: 14 October 2025

Accepted: 4 March 2026

Published online: 18 March 2026

Cite this article as: Wu L., Wang Y., Yang J. *et al.* Application of UAV photogrammetry technology in identifying discontinuities in slopes in the Pulang copper mine. *Sci Rep* (2026). https://doi.org/10.1038/s41598-026-43520-w

Lianrong Wu, Yongran Wang, Jiahong Yang, Bicheng Wang, Sheng Wang, Xinyuan Yang, Xinlong Liu & Zihao Leng

Application of UAV photogrammetry technology in identifying discontinuities in slopes in the Pulang copper mine

Lianrong Wu [1], Yongran Wang [2], Jiahong Yang [1], Bicheng Wang [2], Sheng Wang [1], Xinyuan Yang [2], Xinlong Liu [3,*] and Zihao Leng [3]

[1] Kunming Prospecting Design Institute Of China Nonferrous Metals Industry Co., Ltd., Kunming 650051, China
[2] Yunnan Diqing Non-Ferrous Metal Co., Ltd., Diqing 674408, China
[3] School of Geosciences and Info-physics, Central South University, Changsha 410083, China
* Correspondence: csulxl@csu.edu.cn

Abstract: Identifying discontinuities in high, steep rock slopes is challenging. This study proposes a high-precision geometric feature measurement method for discontinuities on the basis of point cloud data acquired via unmanned aerial vehicle (UAV) photography. The method effectively extracts key parameters, including orientation, trace length, and spacing. The implementation process comprises five main steps. First, principal component analysis (PCA) is used to extract feature information from the point cloud data. Second, the point cloud is preliminarily segmented via a curvature threshold and the density-based spatial clustering with noise (DBSCAN) algorithm. Third, the density peak clustering (DPC) algorithm is adopted to identify cluster centers and divide the discontinuity sets. Fourth, secondary DBSCAN clustering is performed on each discontinuity set to obtain complete individual discontinuities. Finally, geometric characteristics such as orientation, trace length, and spacing are measured on the basis of the principles of analytic geometry. The experimental results show that the orientation deviation calculated by this method is within an acceptable range and that the proposed method has higher computational efficiency than the traditional DPC method. The influence of random fracture networks (DFNs) on the stability of rock slopes was investigated via discrete element numerical simulations.

Keywords: point cloud; discontinuity; semiautomatic extraction; UAV

1. Introduction

The collapse of rock masses is a common hazard in engineering and public safety and is usually controlled by discontinuities [1]. Among these factors, the orientation, spacing, and trace length of discontinuities are key factors affecting the stability of rock masses [2]. After a rock mass has undergone discontinuity development, weathering, erosion, and spontaneous collapse over a long geological period, some of the discontinuities hidden within the rock mass have been exposed [3]. Therefore, by observing and studying these exposed discontinuities from the outside, the internal structure of the rock mass can be restored, and its stability can be analyzed [4].

Noncontact measurement technology and point cloud recognition, segmentation and clustering algorithms are crucial not only for the practical and theoretical development of geotechnical engineering but also for promoting the cross-integration of multiple disciplines and technological innovation. Rock mass discontinuity (such as joints, faults, bedding) identification and analysis are important tasks in geotechnical engineering and directly affect engineering stability evaluation and warning of hazards[5]. The noncontact measurement technology of a rock mass acquires the geometric characteristics of the rock mass without direct contact with its surface through methods such as remote sensing, lasers and electromagnetic-based techniques[6]. These technologies are widely applied in geotechnical engineering, geological disaster monitoring and resource exploration because of their advantages of high efficiency, safety and adaptability to complex environments[7]. Satellite remote sensing technology has wide coverage and is suitable for large-scale structural analysis at the macroscopic level. However, its relatively low resolution makes it difficult to identify small-scale joints and fractures in rock masses[8]. The data collected via 3D laser scanning are relatively comprehensive. Moreover, the roughness and connectivity rate of discontinuities can be quantified. However, the equipment is relatively expensive, and the quality of point cloud data collected in densely vegetated areas has decreased[9,10]. Unmanned aerial vehicle (UAV) photogrammetry technology refers to the use of UAVs equipped with high-resolution cameras to obtain images of the rock mass surface and generate point cloud models through three-dimensional

reconstruction. It can quickly obtain high-precision three-dimensional data and is suitable for steep or dangerous areas. It is commonly applied in the stability analysis of open-pit mine slopes and emergency investigations of geological disasters, but its effectiveness is poor in vegetated areas[11,12].

With the development of 3D laser scanning and UAV photogrammetry technology, point cloud data have become an important data source in the research of rock mass discontinuities[13]. The identification of rock mass discontinuities aims to extract geometric parameters, such as orientation, spacing, and roughness. Traditional methods rely on manual investigation, whereas modern technology combines point cloud processing algorithms to achieve automated analysis. At present, point cloud processing algorithms can be divided into traditional methods, deep learning-driven methods and density clustering methods. The traditional methods include k-means, random sampling consensus (RANSAC), and region growing (RG) algorithms. The k-means algorithm is widely used and has the advantages of convenient and fast calculation. However, it is sensitive to noise points and cannot handle nonconvex cluster structures[14,15]. The RANSAC algorithm has strong noise resistance and a large applicable scale, but it is rather difficult to handle curved surface structures[16,17]. The RG algorithm can adapt to the surface structure, but the growth threshold is relatively sensitive, and the parameter tuning process is cumbersome and complex[15]. Deep learning-driven methods[18,19] are emerging approaches that are well suited for complex geological settings and offer strong capabilities in identifying discontinuities. For example, [200] proposed a method that combines multiview image enhancement with a CNN to achieve high-precision structural plane detection on basalt columns. However, these methods require large training datasets and significant computational resources, which may limit their practical applicability[21]. Density clustering methods include density-based spatial clustering of applications with noise (DBSCAN) and density peak clustering (DPC) methods. The DBSCAN method divides clusters on the basis of point density and identifies high-density regions as discontinuities. It is often applied in individual discontinuity identification, and noise points can be separated without presetting the number of clusters[22,23]. The DPC method determines the clustering centers through local density (ρ) and relative distance (δ). It is applicable to the automatic grouping of advantageous discontinuity sets (such as multiset joint systems), but at the same time, this method has high time complexity and low efficiency when dealing with large-scale point clouds[24,25]. These two methods have high computational efficiency and a strong ability to distinguish and identify discontinuities and are more suitable for the research field of this study, providing a feasible approach for measuring and monitoring high and steep rock slopes that are difficult for humans to reach. Moreover, some studies are dedicated to obtaining data through low-cost platforms such as smartphones. Ozturk et al.[26] successfully utilized smartphone photos for photogrammetry, generating point clouds and applying them to structural plane occurrence measurement and kinematic analysis, demonstrating the feasibility of a low-cost technical route. However, such methods still have room for improvement in terms of the degree of automation and intelligence of the subsequent processing of point clouds, and they also need to handle point cloud models that may contain hundreds of thousands or even millions of points.

In response to the aforementioned research gaps, the main innovation of this study lies in the proposal of a hierarchical clustering framework. The core idea of this framework is as follows: By introducing curvature threshold prefiltering and dual DBSCAN clustering strategies, the original large-scale point cloud is "reduced in dimension" and preliminarily organized. Only the DPC algorithm is applied to the representative subset for the division of dominant groups, thereby maintaining the accuracy of DPC grouping while significantly avoiding the high computational cost caused by directly operating on the entire point cloud. This study uses the high-angle steep slope of the Pulang copper mine in Yunnan Province, which has dense vegetation and rugged terrain, as an example to verify the effectiveness of this framework in efficiently identifying structural face groups and extracting complete individuals and geometric parameters. Furthermore, the extracted parameters are used to simulate discrete fracture networks to evaluate the stability of the slope. This study aims to provide a practical technical solution that balances accuracy and efficiency for rock mass structure surveys in similar high-risk and inaccessible areas.

2. Research area

2.1. Overview of the research area

The Pulang copper mine area is located in the northeastern part of Shangri-La County, Diqing Tibetan Autonomous Prefecture, northwest Yunnan Province. It is situated on the southeastern edge of the Qinghai–Tibet Plateau and the northeastern part of the Hengduan Mountains in northwest Yunnan, close to the Three Parallel

Rivers World Natural Heritage Reserve. The mine area is sparsely populated, with high mountains and dense forests. The vegetation coverage has a significant effect on the measurement work of this study.

The eastern slope of the surface movement area—near the East Plant—features steep terrain, with an average slope angle of approximately 45°. On-site investigations, UAV-based surveys, and close-range photogrammetry revealed that a large area of bedrock is exposed on this slope and that the rock mass is highly fractured, with well-developed joints and fissures. A schematic diagram of the research area is shown in Fig. 1. Fig. 1a and 1b are schematic diagrams of the location of the research area. Fig. 1c shows an overall view of the eastern slope in the surface movement area of the Pulang copper mine. The topography and geomorphology of the eastern slope in the surface movement area of the Pulang copper mine are shown in Fig. 1d.

The first ore body is located on the eastern side of the mine, with its extraction zone situated at the foot of the mountain. Mining operations in this area involve deep excavation, with a cutting depth approaching 100 m, posing a significant risk of rock mass instability or even gravity-induced collapse. Therefore, it is necessary to carry out early-stage investigations and model potential collapse scenarios, evaluate the affected area and associated risks, and implement appropriate monitoring technologies and control measures.

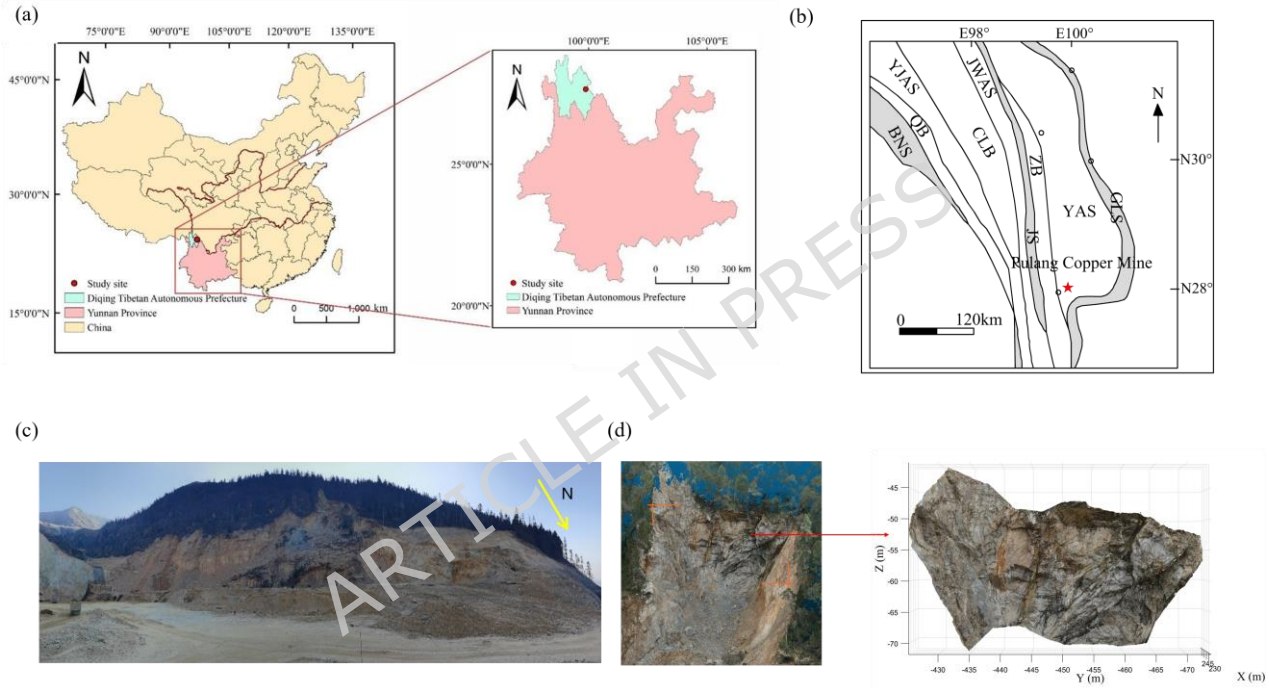

Fig. 1. Schematic diagram of the research area. (a)(b) The schematic diagrams of the location of the research area. (c) The overall view of the eastern slope in the surface movement area of the Pulang copper mine. (d) The topography and geomorphology of the eastern slope in the surface movement area of the Pulang copper mine.

2.2 Data acquisition

The data collection in this study was conducted with a DJI M300 RTK unmanned aerial vehicle equipped with a Zenmuse P1 lens, with the aim of comprehensively obtaining the overall topography of the mountain around the collapse pit and providing high-precision point cloud data for subsequent discontinuity analysis. The UAV system offers high positioning accuracy and stable flight performance and is capable of capturing wide areas at relatively high altitudes. By flying around the collapse pit, a series of overlapping aerial images were obtained to generate a complete point cloud.

However, the eastern slope of the study area is heavily vegetated, resulting in limited exposure of bare rock surfaces and discontinuities. In many areas, the rock mass is obscured by dense vegetation, particularly in UAV-derived point clouds. Therefore, it is necessary to conduct a preliminary segmentation and processing of point cloud data to ensure the subsequent identification and analysis of discontinuities [27].

On the basis of a comprehensive analysis of the point cloud covering the entire study area, a representative region with relatively well-exposed rock surfaces was selected for detailed investigation, as shown in Fig. 1d. These exposed rock masses provide a reliable basis for the subsequent identification of discontinuities. However, due to residual vegetation in certain regions, more detailed manual segmentation treatment has been carried out to

remove nonrock elements. Through the manual filtering process, vegetation-covered areas were excluded, resulting in a cleaned point cloud that contains only the relevant rock mass information. The cleaned point cloud, as shown in Fig. 1d, serves as the foundation dataset for the accurate identification of rock mass discontinuities and extraction of their geometric parameters.

Table 1. Detailed specification parameters of the UAV

Dimensions	Dimensions (unfolded, excluding blades): 810*670*430 mm (length*width*height) Dimensions (folded, including blades): 430*420*430 mm (length*width*height)
Symmetrical motor axle spacing	895 mm
Weight (including the lower-mounted single pantilt base)	Weight (excluding battery): 3.6 kg Weight (including two batteries): 6.3 kg
Maximum load	2.7 kg
Maximum takeoff weight	9 kg
Working frequency	2.4000-2.4835 GHz 5.725-5.850 GHz
Effective isotropic radiated power	2.4000-2.4835 GHz: 29.5 dBm(FCC); 18.5 dBm(SRRC); 18.5 dBm(MIC) 5.725-5.850 GHz: 28.5 dBm(FCC); 12.5 dBm(SRRC); 28.5 dBm(MIC)
Hovering accuracy	Vertical: ±0.1 m (normal operation of visual positioning) ±0.5 m (normal operation of GPS) ±0.1 m (normal operation of RTK) Horizonal: ±0.3 m (normal operation of visual positioning) ±1.5 m (normal operation of GPS) ±0.1 m (normal operation of RTK)
RTK position accuracy	During RTK FIX: 1 cm + 1 ppm (horizonal) 1.5 cm + 1 ppm (vertical)

Table 2. Detailed specification parameters of the camera

Dimensions	198*166*129 mm
Sensor	Sensor size (photo): 35.9*24 mm (full frame); Sensor size (maximum video size): 34*19 mm; Effective pixels: 45 million; Pixel size: 4.4μm
Image size	3:2 (8192*5460)
Minimum photo interval	0.7 seconds
Shutter speed	Mechanical shutter: 1/2000–1 seconds; Electronic shutter: 1/8000–1 seconds
Aperture range	f/2.8-f/16
ISO scope	Photo: 100-2560 Video: 100-2560

3. Methodology for Discontinuity Identification and Parameter Extraction

3.1 Point cloud characteristic processing

The methodology consists of four main steps, as illustrated in Fig. 2. First, data acquisition is performed using UAV photogrammetry to collect high-resolution point-cloud data covering the entire site, especially the mountain slopes above the collapse pit, ensuring full spatial coverage and required accuracy.

Second, discontinuity identification is carried out on the point cloud using the method proposed in this study.

Third, parameter extraction is conducted, where key geometric parameters--including orientation, trace length, and spacing--are derived from the identified discontinuities. These parameters serve as critical inputs for

discontinuity network modeling. Finally, numerical simulation is performed by constructing a discrete fracture network (DFN) using the extracted parameters, which is then embedded into a numerical rock mass model to simulate the mechanical behavior of the outcropping slope under self-weight.

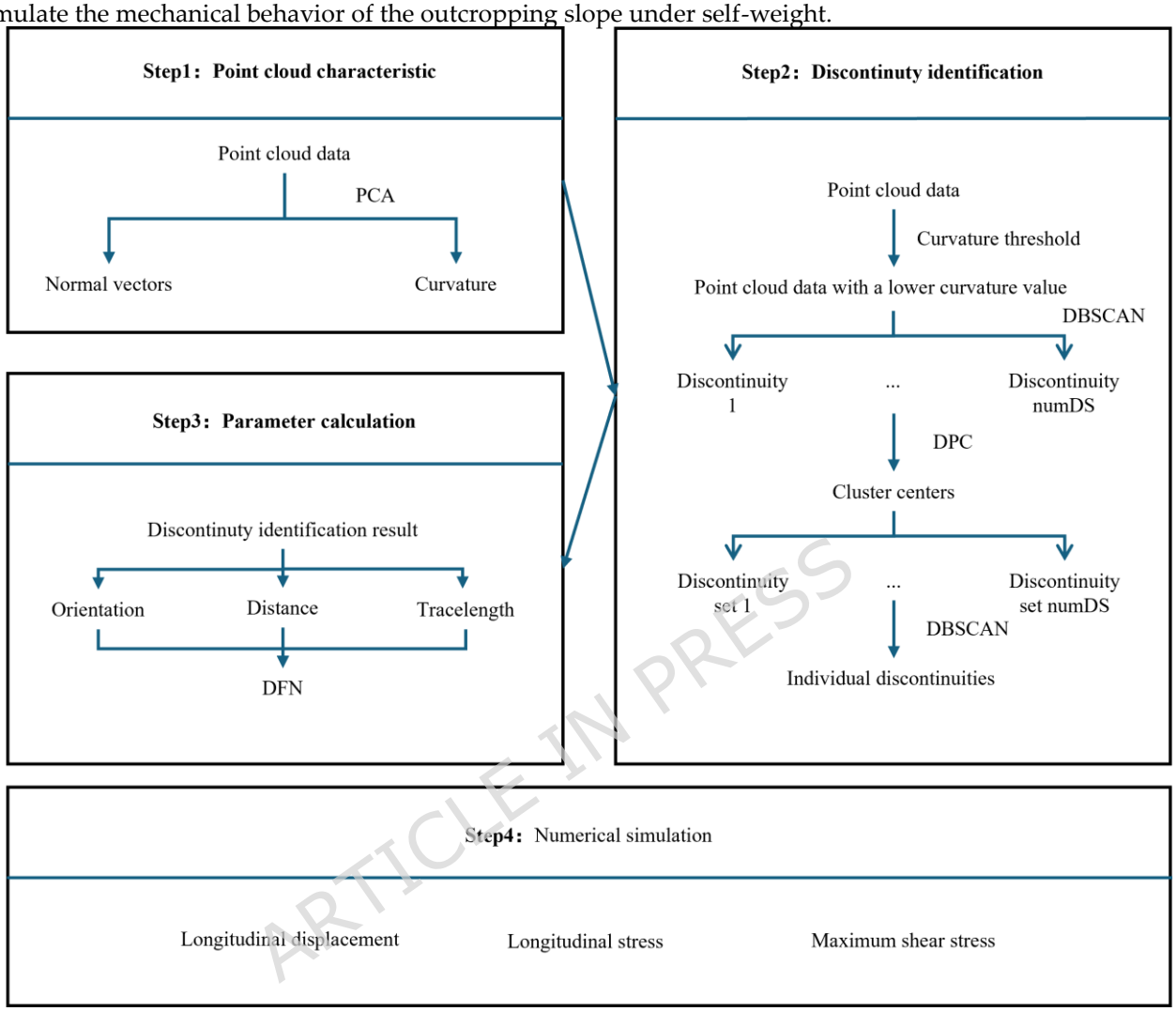

Fig. 2. The flowchart of the method.

DBSCAN identifies clusters by locating regions of high point density and distinguishing them from surrounding sparse areas, which are treated as noise. In this study, the point normal vector and curvature are selected as the recognition features. The normal vector is defined as the normal of the best-fit plane formed by the k points adjacent to the point. Principal component analysis (PCA) is used to process the features of the point cloud. PCA is a linear dimensionality reduction method that projects high-dimensional data onto a lower-dimensional subspace via orthogonal transformation, preserving the directions with the greatest variance. Its general principle is as follows:

For any point P_i in the point cloud, calculate its Euclidean distance from another point P_j and select the k points nearest neighbors to form a local point set Q_i.

$$d(i,j) = \sqrt{(x_i - x_j)^2 + (y_i - y_j)^2 + (z_i - z_j)^2} \quad (1)$$

The covariance matrix C of the point set Q_i is calculated as:

$$C = \begin{bmatrix} Cov(X,X) & Cov(X,Y) & Cov(X,Z) \\ Cov(Y,X) & Cov(Y,Y) & Cov(Y,Z) \\ Cov(Z,X) & Cov(Z,Y) & Cov(Z,Z) \end{bmatrix} \quad (2)$$

Then, the eigenvalues λ_n and eigenvectors v_n of the covariance matrix C are calculated as follows:

$$\lambda_n v_n = C v_n \quad (3)$$

Assuming that $\lambda_1 \geq \lambda_2 \geq \lambda_3$, the eigenvector v_3 corresponding to λ_3 is the normal vector of point P_i. The curvature equals the quotient of the minimum eigenvalue λ_3 to the sum of the eigenvalues.

The estimation of the point normal vector is sensitive to the choice of the parameter k used for selecting nearest neighbors. When the value of k is too small, the number of nearest points selected is insufficient, and the obtained point normal vectors may exhibit large fluctuations even in locally continuous regions. When the value of k is too large, the nearest point selected may be the noise point or the point that is far away, introducing significant errors in the estimated normal vectors of the query point. Therefore, choosing an appropriate k value is crucial for ensuring reliable normal estimation. After many tests, k=40 was selected as the optimal value.

3.2 Point cloud segmentation

Since the DBSCAN algorithm performs well when there is a certain interval between clusters, it is necessary to preprocess the point cloud data before conducting the identification of discontinuities. The curvature of points located near the intersection line caused by discontinuity intersections is relatively large. Therefore, the points near the intersection line can be eliminated by setting a curvature threshold to obtain independent clusters for the next step of discontinuity identification.

The basic idea of the DBSCAN algorithm is to start from any unvisited core point, recursively merge all density-reachable points to form clusters, and points that cannot be connected to any core point are marked as noise. It relies on two parameters: the neighborhood radius ε and the minimum number of points within the neighborhood minpts. The calculation steps are as follows:

As shown in Fig. 3, the DBSCAN algorithm traverses all unvisited points and randomly selects one point as the initial point. The algorithm then detects the number of points in the ε neighborhood around the selected point. If the number of neighbors reaches the preset threshold minimum, the selected point is marked as a core point, and the points in the neighborhood are grouped into a cluster. If the number of points in the neighborhood is less than the minimum number of points, the point is not considered a core point and is temporarily skipped. The process continues by recursively expanding the cluster from the core point, merging all density-reachable points until no new points can be added. This procedure is repeated until all the points in the dataset have been visited, completing the division of the discontinuities.

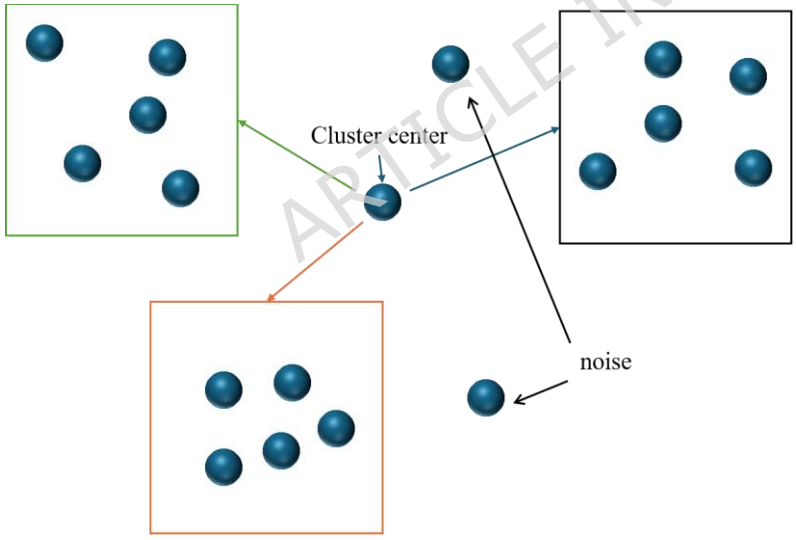

Fig. 3. Schematic diagram of DBSCAN.

3.3 Identification of discontinuity sets

After the point cloud is initially segmented into individual discontinuities via DBSCAN, the DPC algorithm is employed to further group individual discontinuities on the basis of the similarity of normal vectors. The principle of the DPC clustering algorithm is as follows**Error! Reference source not found.**:

First, the DPC algorithm is based on two basic assumptions:

1. There are low-density points distributed around the cluster center.
2. The cluster centers belonging to different clusters are relatively far apart.

On the basis of these two basic assumptions, the DPC algorithm calculates the local density ρ_i of each point via either the truncated kernel (Equation (4)) or the Gaussian kernel (Equation (5)).

$$\rho_i = \left|\{d_{ij} < d_c\}\right| \quad (4)$$

$$\rho_i = \sum_{i \neq j} \exp\left[-\left(\frac{d_{ij}}{d_c}\right)^2\right] \quad (5)$$

where d_c is the predefined cutoff distance and where d_{ij} is the distance between point i and any point j. Since each individual discontinuity is represented by a normal vector, the distance d_{ij} is defined by the acute angle between their normal vectors, which more accurately reflects their similarity. Among the two kernel functions, the truncated kernel is more suitable for large-scale datasets, whereas the Gaussian kernel performs better for smaller datasets.

The relative distance δ_i of each point i is calculated as the distance to the nearest point with a higher density (Equation (6)):

$$\delta_i = \min_{\rho_i < \rho_j} d_{ij} \quad (6)$$

Then, on the basis of the calculation results obtained above, a decision graph (ϱ - δ) is drawn, and the top n points with the highest values of the two variables are manually selected as the clustering centers, where n corresponds to the number of discontinuity sets.

Each point in the dataset has an associated normal vector. The acute angles between the normal vector of each point and the cluster centers are calculated, and each point is assigned to the cluster with the smallest angle, resulting in the classification of all points into respective discontinuity sets.

3.4 Individual discontinuity extraction

While the discontinuities of different orientations were grouped, the initial point cloud data were also divided into four sets. Given that the initial segmentation—due to curvature filtering—may not capture the full number or extent of individual discontinuities, a second round of DBSCAN clustering was necessary within each discontinuity set. This step aims to extract complete individual discontinuities.

3.5 Parameter calculation

3.5.1 Orientation

The orientations of discontinuities include dip directions and dips. Dip direction α is the clockwise angle between the horizontal projection of the discontinuity normal vector and the geographic north direction (the positive direction of the Y-axis), and its calculation formula is as follows:

$$\alpha = \begin{cases} 90° - tan^{-1}\frac{u_y}{u_x}, u_x > 0 \\ 270° - tan^{-1}\frac{u_y}{u_x}, u_x < 0 \end{cases} \quad (7)$$

The dip β is the angle between the discontinuity plane and the horizontal plane, and its calculation formula is as follows:

$$\beta = cos^{-1}|u_z| \quad (8)$$

where u_x, u_y and u_z represent the components of the unit normal vector of the discontinuity along the x, y and z axes, respectively.

3.5.2 Trace length

On a rock slope, the intersection line of the discontinuity and the open surface is called a trace, and the actual length of the trace is the trace length. In previous studies, the line connecting the two points farthest apart on the intersection line was usually regarded as the trace length. To increase computational efficiency, this traditional simplified method is directly adopted to calculate the trace length. However, the limitations of this method must be noted. Essentially, this method simplifies complex curved spatial lines that may be bent or curved into straight line segments between their endpoints. Therefore, the "trace length" calculated is always less than or equal to the actual curve length of the trace line. They are equal only when the trace line is an absolute straight line. This leads to an underestimation of the trace length.

3.5.3 Spacing

After the discontinuities are grouped on the basis of their normal vectors, the discontinuities within each set exhibit approximate parallelism. To compute the spacing—defined here as the perpendicular distance between adjacent, near–parallel discontinuities—the following procedure is applied:

First, individual discontinuities within the same set should be adjusted to the average orientation to ensure that they are mutually parallel during the calculation process. This adjustment ensures that all discontinuities in

the set are treated as strictly parallel planes for the purpose of spacing calculation, minimizing the effect of minor within-set scatter.

In the three-dimensional Cartesian coordinate system, the projections of the same set of discontinuities on the plane perpendicular to them are many parallel line segments whose lengths are the lengths of the lines connecting the two points farthest apart on the trace calculated in the previous step. The equation of the straight line in the three-dimensional Cartesian coordinate system can be expressed as:

$$Ax + By + Cz = D \quad (9)$$

In this paper, the method proposed by Cao. et al. 2025 is adopted to calculate and obtain each pair of discontinuities of the calculated spacing in three-dimensional space (Cao et al., 2025). Since the lines in the same set are parallel to each other, they have the same A, B and C in Equation (9), with the only difference being D. Therefore, the discontinuities in the same set can be labeled and sorted according to the value of D, and then the distances between the discontinuities of adjacent serial numbers can be calculated to obtain the spacing data. As shown in Figure 4, the six discontinuities within the same set are named Disset1 to Disset6 according to the value of D. Then, each discontinuity is paired with the nearest discontinuity to calculate the distance between each discontinuity and the nearest discontinuity. For example, Disset2 pairs with two discontinuities, Disset1 and Disset3. However, Disset3 has two discontinuities that are relatively close above it and are both assigned to Disset3 for pairing. Therefore, Disset3 has three discontinuities that pair with it. In summary, in addition to sorting the largest and smallest discontinuities, each discontinuity is paired with at least two nearest discontinuities in the same set.

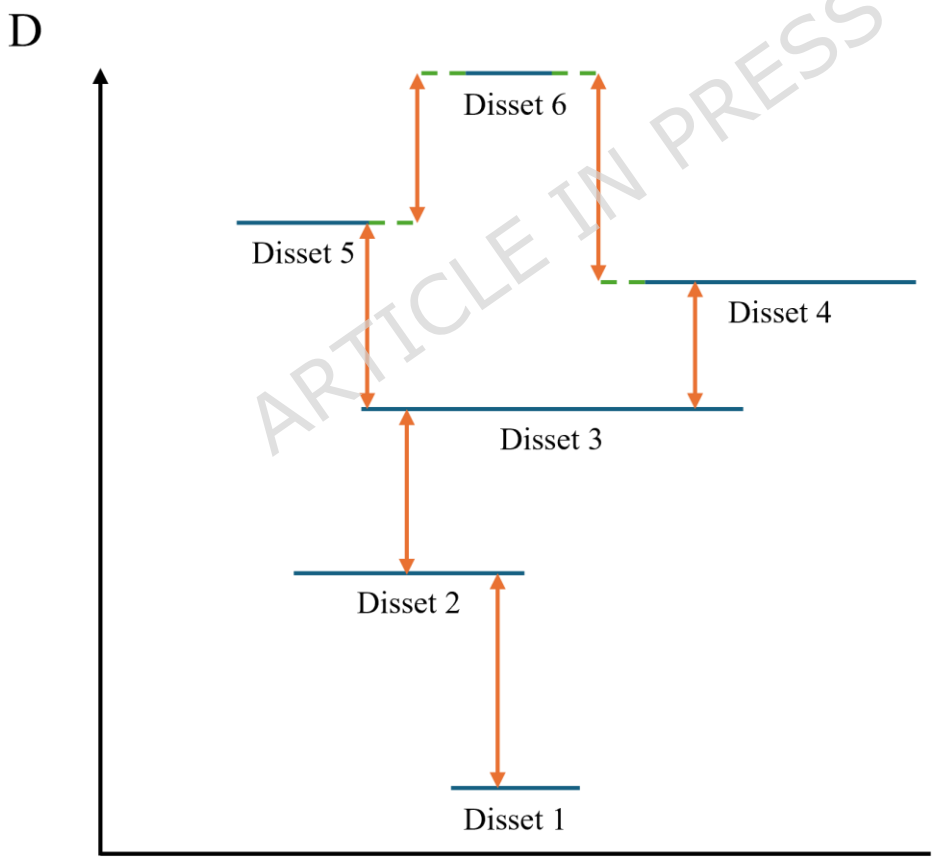

Fig. 4. Scheme of discontinuity pairing.

4 Results

4.1 Calculation results

Fig. 5 shows the calculation results of the normal vectors. Points with similar colors correspond to similar normal vectors, indicating consistent surface orientations. Therefore, the discontinuity of the selected data area can be divided into four sets.

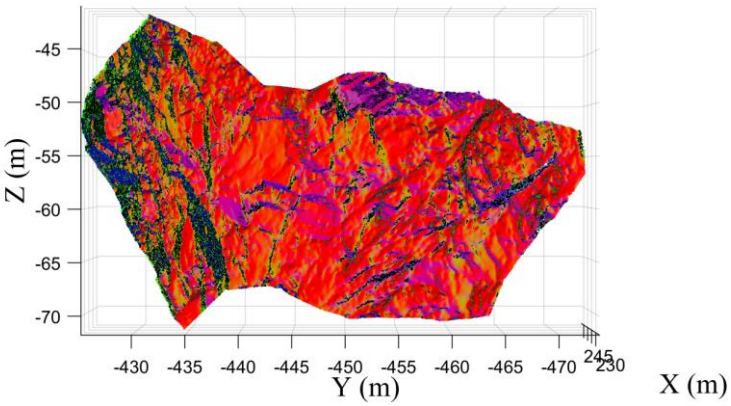

Fig. 5. Normal vectors of the 3D point cloud.

Fig. 6 shows the point cloud data after removing the points with curvature values exceeding the predefined threshold. The points near the discontinuity line have been effectively eliminated, which is conducive to the next DBSCAN clustering work. The selection of the curvature threshold is crucial. When the threshold is too large, there are fewer rejection points, which easily leads to the identification of adjacent intersecting discontinuities as the same discontinuity. When the threshold is too small, there may be a situation where the point cloud density remaining after elimination work on some discontinuities with small exposed areas is too small to be identified as an independent discontinuity. To determine the optimal curvature threshold in this study, we conducted a systematic sensitivity analysis. On the basis of the initial acquisition of the normal vectors of the point cloud and the curvature distribution, we tested a series of thresholds ranging from 0.1--1.0 (with a step size of 0.1) and visually inspected the effect of eliminating intersection points under different thresholds as well as the impact on the subsequent DBSCAN clustering results. The results showed that when the threshold was less than 0.4, significant turning points on the edges of some main structural planes were also eliminated, resulting in a blurred point cloud contour and damage to integrity. When the threshold was greater than 0.6, many points remained in the intersection areas between multiple structural planes, leading to the adhesion of clusters that should have been separated in the initial DBSCAN clustering. When the threshold was 0.5, it had the best effect in the analysis of multiple representative subregions; it could effectively separate adjacent structural planes in space and ensure that the majority of structural planes (including some smaller planes) retained sufficient points for clustering identification.

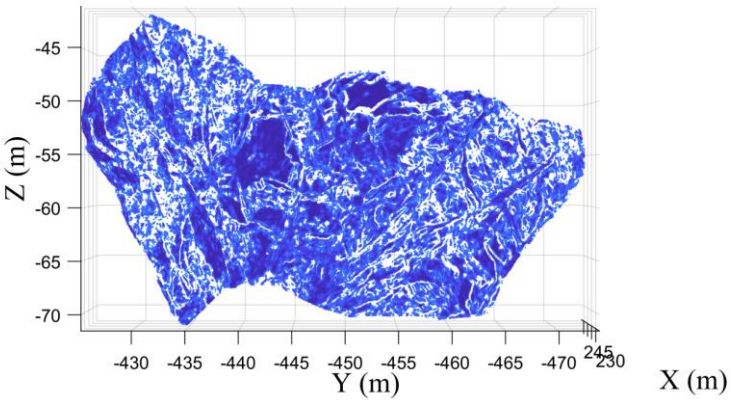

Fig. 6. Process of segmentation.

Fig. 7 shows the result of DBSCAN clustering applied to the preprocessed point cloud. After excluding points near the intersection lines, the remaining data are successfully segmented into different and independent discontinuities. The clustering performance is sensitive to the choice of parameters ε. A value of ε that is too large may cause adjacent discontinuities to merge into one cluster, whereas a value that is too small may result in oversegmentation or failure to detect clusters. To determine the optimal parameters applicable to the point cloud data of this study, we conducted a parameter sensitivity test. The test was based on a point cloud that had undergone curvature threshold preprocessing. First, an empirical initial value of minPts (20) was fixed, which usually effectively filtered out random noise points. A series of ε values (0.05, 0.08, 0.1, 0.15) were subsequently systematically tested. Through visual inspection of the initial DBSCAN clustering results under different ε values and combination with indicators such as the number of clusters and the continuity of points within each cluster, a comprehensive evaluation was conducted. When $\varepsilon \leq 0.05$, the clustering results revealed a significant oversegmentation phenomenon, and many clear plate-like structural planes were split into multiple small fragments. When $\varepsilon \geq 0.1$, an undersegmentation trend begins to appear, and some spatially adjacent, structurally similar but with minor intervals, structural planes are merged. When $\varepsilon = 0.08$, the clustering results were the most ideal: it could identify each independently exposed structural plane as a single cluster and effectively distinguish different structural planes that are spatially adjacent.

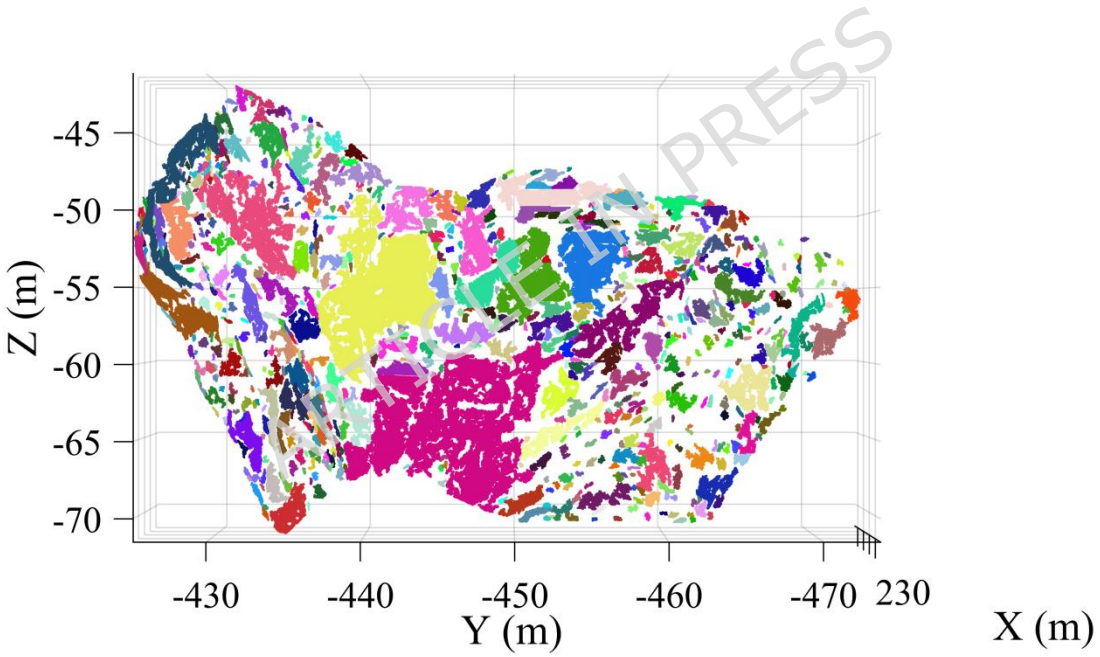

Fig. 7. Results of the first DBSCAN application.

Fig. 8 shows the normal vectors of each cluster obtained via DBSCAN. The red dots represent the cluster centers obtained from these normal vectors via the DPC algorithm.

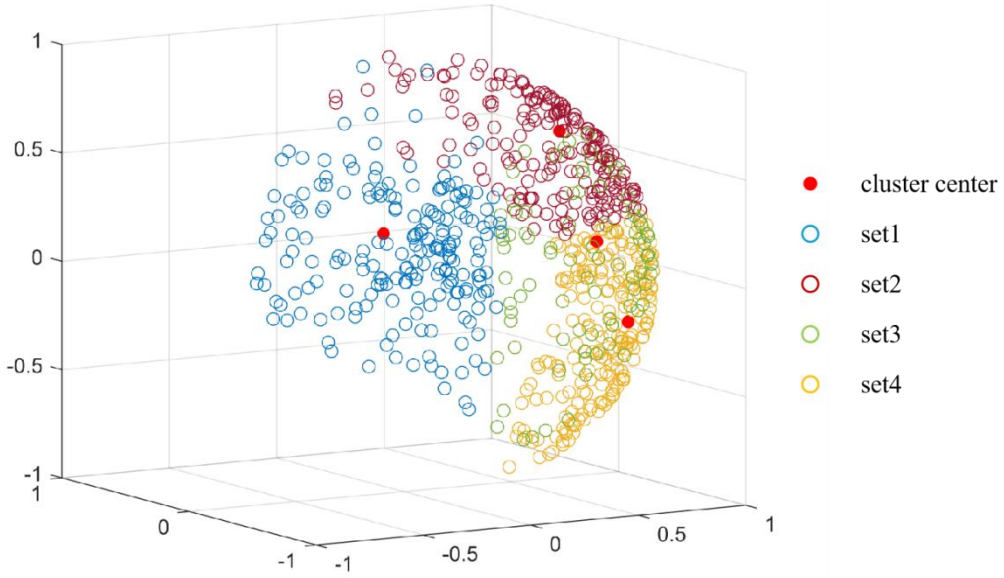

Fig. 8. Normal vector distribution.

Fig. 9 shows that four sets of discontinuity sets with different orientations were obtained, and the specific distributions of their orientations are shown in Fig. 9. Within each set, the discontinuities are approximately parallel and exhibit spatial separation from one another. When the DPC algorithm is used to divide the structural planes, the determination process of the cluster centers involves certain subjective judgments. This step may affect the objectivity and repeatability of the grouping results. To reduce the uncertainty caused by subjectivity, this study followed clear geological and geometric criteria when selecting. First, the cluster centers should significantly deviate from the low-density areas and be separated from each other in space. Second, the direction of their normal vectors should be consistent with the main structural plane trend observed in three-dimensional point cloud rendering. Although a certain degree of artificial judgment was introduced, this method was proven to be effective in this study, successfully identifying four structural plane groups with clear geological significance.

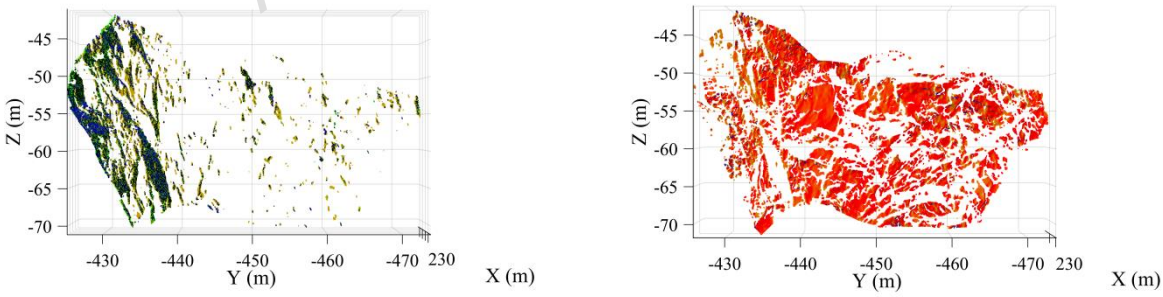

(a) (b)

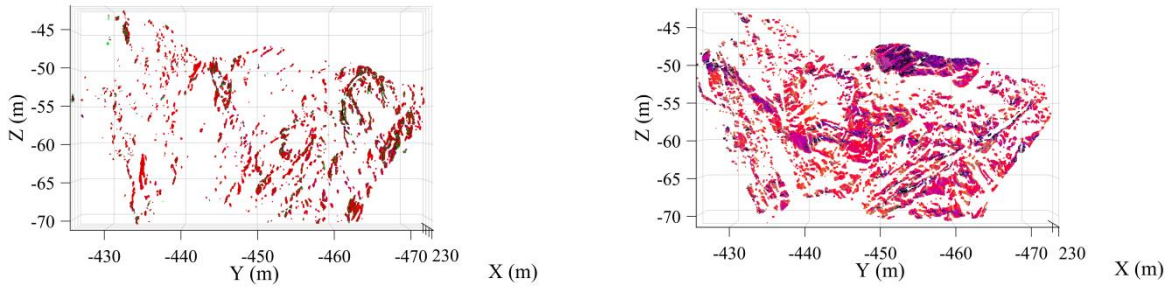

(c) (d)

Fig. 9. Results of orientation calculation: (a) set1; (b) set2; (c) set3; (d) set4.

As shown in Fig. 10, the point cloud data divided into four sets have undergone a second, refined DBSCAN clustering, achieving further division of the independent discontinuities within the sets and providing data for the next parameter calculation.

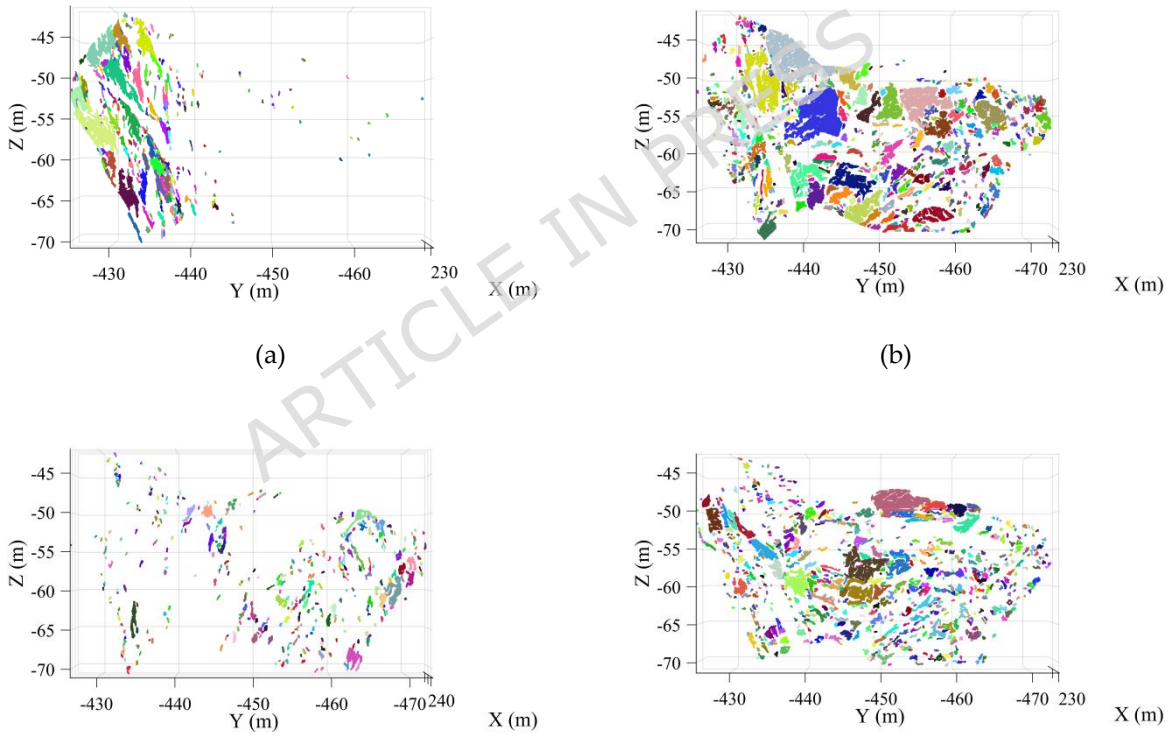

(a) (b)

(c) (d)

Fig. 10. Results of the first DBSCAN application.

Table 3 and Fig. 11 present the orientations of the four identified discontinuity sets, with their mean dip and dip direction values as follows: Set 1 (70.58°/94.85°), Set 2 (76.26°/33.12°), Set 3 (79.78°/276.92°), and Set 4 (61.64°/83.15°). Among them, Sets 2 and 3 exhibit steep dips in nearly opposite directions, forming a typical conjugate relationship indicative of shear-induced jointing under compressive stress. Sets 1 and 3 intersect at a high angle, likely forming an orthogonal joint system that influences potential block separation and failure. In addition to orientation, the trace length and spacing were also calculated for each set.

The trace length statistics indicate that Sets 1 and 2 present longer average trace lengths with noticeable variability, suggesting a wide range of discontinuity sizes, whereas Set 3 is characterized by generally shorter and more uniformly sized discontinuities. The spacing statistics reveal that Set 4 features more closely spaced discontinuities, indicating a higher discontinuity density, whereas Set 3 features more widely spaced discontinuities. This variation in trace length and spacing among the sets reflects the complexity of the

discontinuity network and implies varying block sizes and connectivity, which are critical factors influencing the mechanical behavior and stability of the rock mass.

Table 3. Parameters of the four sets of discontinuities

Set	Number of discontinuities	Dip/dip direction(°)	Trace length(m)		Spacing(m)	
			μ	σ	μ	σ
1	548	70.58/94.85	1.0042	1.2211	0.4699	0.4970
2	291	76.26/33.12	1.0633	1.3731	0.4479	0.4574
3	278	79.78/276.92	0.7325	0.5633	0.5216	0.7126
4	699	61.64/83.15	0.8683	0.8047	0.3703	0.3723

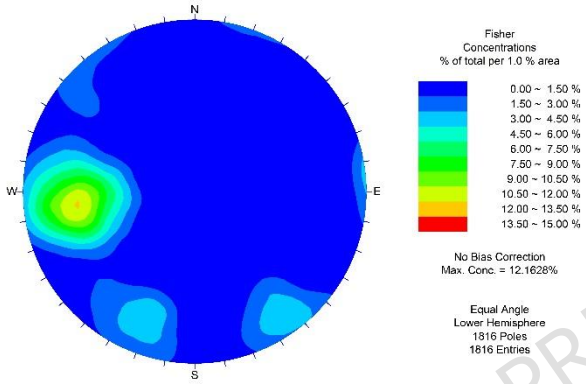

Fig. 11. Discontinuity orientation.

Owing to the high altitude and steep slopes of the study area, combined with the frequent rockfalls caused by ongoing mining activities, manual access to the site for direct measurement of discontinuities is both difficult and unsafe. Consequently, traditional field survey methods for obtaining discontinuity data are impractical. Therefore, this paper chooses to manually fit some discontinuities through point cloud data imported into the software Cloudcompare. The manual fitting was performed using the Facet plugin, which allows users to select points belonging to a discontinuity plane and fit a plane to them, thereby obtaining its orientation. The results from this manual method were then compared with those calculated by the proposed algorithm.

Table 4 compares the orientations obtained via manual fitting and calculated via the proposed method for several representative discontinuities. The results demonstrate close agreement between the two approaches. Specifically, the maximum deviation observed is 5.65° in the dip direction for discontinuities 41 and 4.59° in the dip direction for discontinuity 13, whereas most other discontinuities exhibit much smaller differences. However, this deviation is within an acceptable range given the inherent uncertainties associated with manual fitting and the roughness of discontinuities. Overall, the above results prove the effectiveness of extracting discontinuities from point clouds via the method proposed in this paper. This confirms that the method can effectively capture key geometric parameters of discontinuities, providing a basis for rock mass stability analysis in challenging field conditions where conventional surveying is limited.

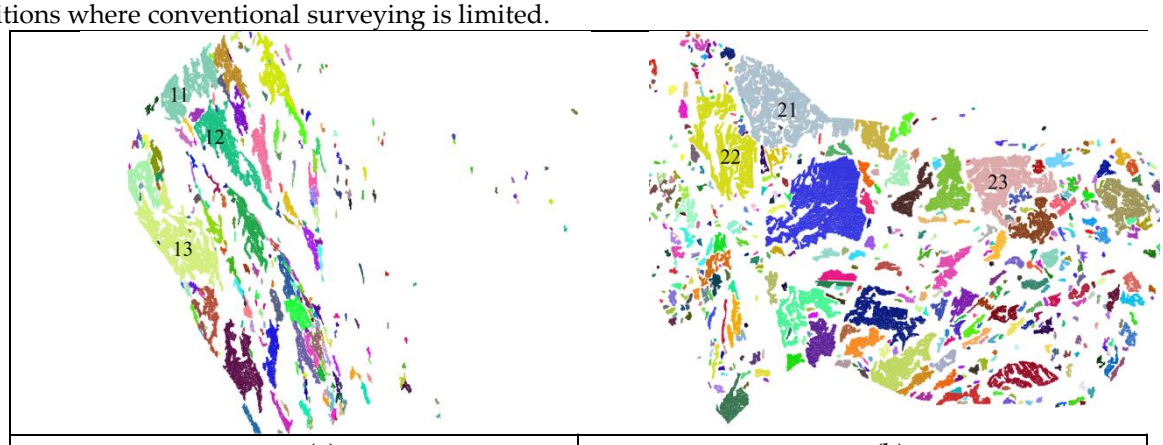

(a) (b)

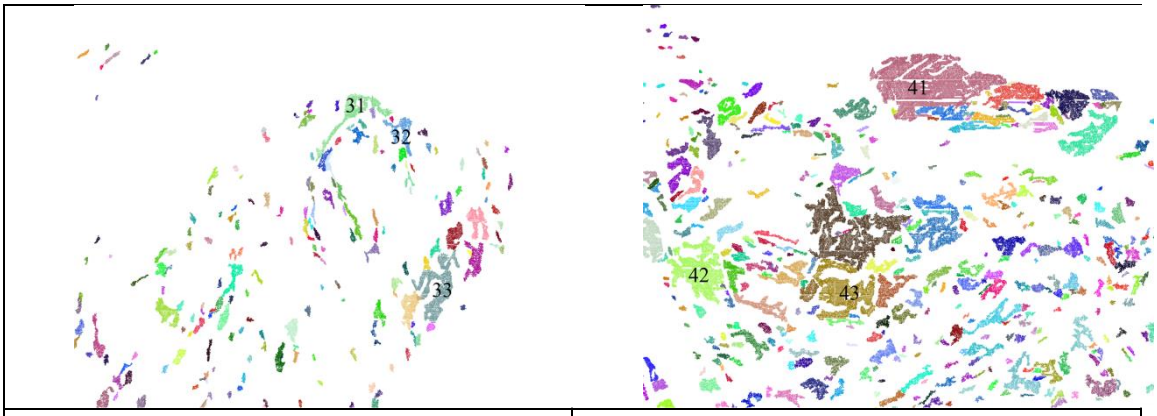

Fig. 12. Several representative discontinuities for manual fitting. (a) Discontinuity 11--13. (b) Discontinuity 22--23. (c) Discontinuity 31--33. (d) Discontinuity 41--43.

Table 4. Comparison between the proposed method and the cloudcompare results

Discontinuity ID	Dip/dip direction(°)		Deviation(°)
	Proposed method	Cloudcompare	
11	70.52/94.63	73.25/92.65	2.73/1.98
12	72.69/95.32	74.45/93.21	1.76/2.11
13	71.93/94.37	72.75/94.69	0.82/0.32
21	76.66/33.90	80.54/36.23	3.88/3.89
22	75.37/34.12	79.36/34.31	3.99/0.19
23	74.98/32.39	81.51/36.98	2.71/4.59
31	79.12/276.32	83.58/276.56	4.46/0.24
32	78.54/275.91	82.56/278.36	4.02/2.45
33	76.92/262.32	80.96/260.14	4.04/2.18
41	61.23/83.89	66.98/80.66	5.65/3.23
42	54.39/80.52	59.32/76.84	4.93/3.68
43	62.55/85.92	60.78/90.14	1.77/4.22
	Average deviation		4.53/3.23

4.2 Numerical simulation

The parameters calculated by the above methods can be applied to generate a random fracture network for the stability of rock slopes**Error! Reference source not found.**. On the basis of the geological exploration report of the Pulang copper mine project and discontinuity data collected from point clouds, a preliminary numerical simulation analysis of rock slopes with random fracture networks was carried out to evaluate the stability of the slopes in the study area and predict the areas where rockfalls and collapses may occur. The discrete element method (DEM) was employed for numerical modeling because of its proven effectiveness in simulating the mechanical behavior and movement of discrete, irregular rock blocks**Error! Reference source not found.** and is particularly suitable for simulating the conditions of rock slopes and joint fissures such as those in this study. The parameters used for the numerical simulation are shown in Table 5:

Table 5. Parameters used in the numerical simulation

Parameters	Rock	Joint
Density(kg/m^3)	2650	/
Elastic modulus(GPa)	2.5	/
Poisson	0.26	/
Cohesion(MPa)	15	5.2

Tensile strength(MPa)	5.5	3.2
Internal friction angle(°)	42	38
Nomal stiffness(kN/m)	/	4×10^4
Shear stiffness(kN/m)	/	4×10^4

To realistically simulate the force conditions of the slope in the study area under self-weight, a surface-fitting technique was applied to the point cloud data of the slope surface, enabling the construction of a high-fidelity slope model. This approach allows the reconstructed model to closely reflect the actual topography of the study area (Fig. 13). On this basis, the average density of the grid is approximately 0.65 per square meter. The determination of this size takes into account both computational efficiency and the ability to analyze the main rock structure to ensure that stress and deformation can be reasonably represented at the unit scale. The boundary conditions of the model are set as follows: the bottom of the model is set as a completely fixed constraint to simulate the rigid support of the deep bedrock; the normal displacement constraints are applied around the model to approximately simulate the constraint effect of the surrounding rock; and the top of the model and the cliff face are set as free boundaries, thereby allowing the rock mass to deform and move under the action of its own weight.

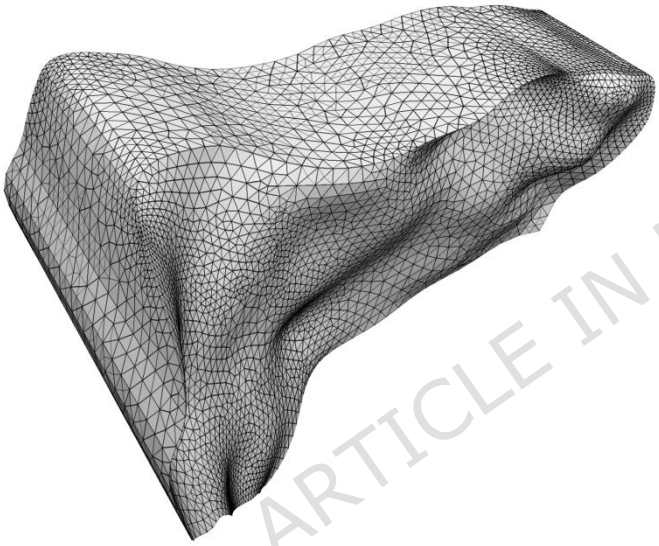

Fig. 13. Model and grids.

A discrete fracture network (DFN) model was then generated using the geometric parameters—orientation, trace length, and spacing—of the four identified discontinuity sets. The DFN simulates fracture development within the rock mass on the basis of the statistical characteristics of the discontinuities (Fig. 14a). Fig. 14b shows a schematic diagram of the discontinuities cut by this group of DFNs on the surface of the cube. The establishment of the DFN model is mainly based on the average occurrence patterns of the four discontinuity sets calculated in the previous text. To determine the most appropriate statistical distribution for DFN modeling, Kolmogorov--Smirnov (K--S) tests were performed on the trace length data and spacing data of each set. The trace lengths and spacings were best fitted by lognormal distributions. These statistical models were then used to generate the DFN, ensuring that the synthetic fracture network accurately reflects the natural variability observed in the field.

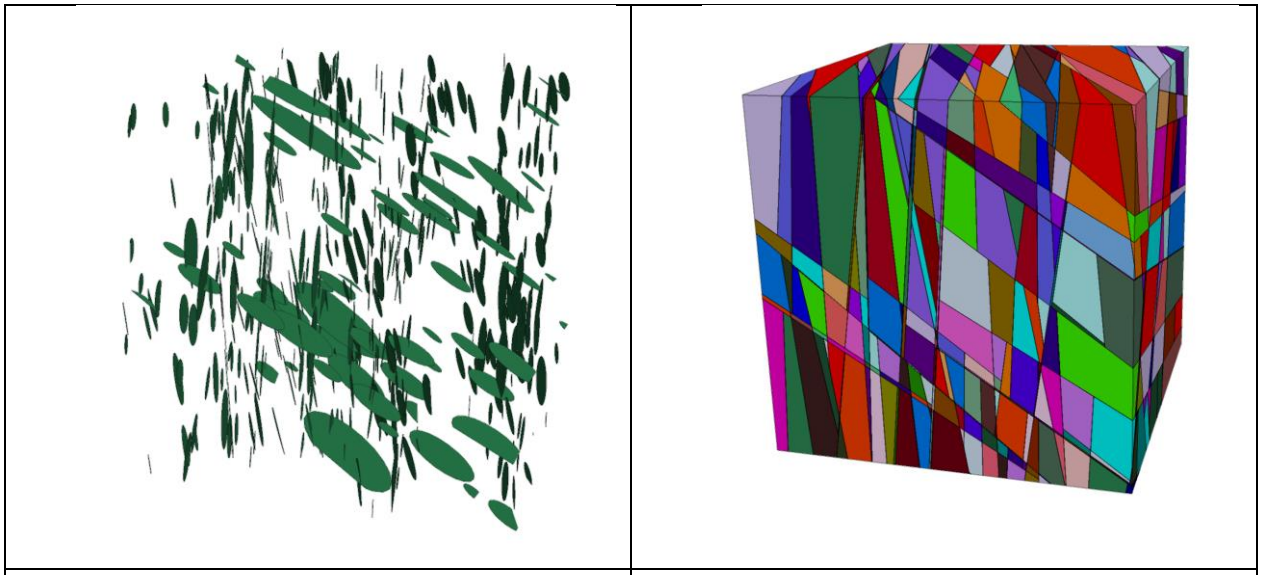

(a) (b)

Fig. 14. DFN model: (a) DFN framework; (b) schematic diagram of a cube block cut by the DFN

The established DFN model was embedded into the model of the rock slope in the study area. The parameters of the rock mass and joints were set according to Table 5, and the numerical simulation was carried out under self-weight conditions, as shown in Fig. 15. Fig. 15a, c, and e represent the control group without the DFN, whereas Fig. 15b, d, and f represent the experimental group incorporating the DFN. The longitudinal displacement, longitudinal stress, and maximum shear stress of the rock slope were compared. Under the condition of only being affected by self-weight and without the influence of the DFN, the longitudinal displacement of the rock slope is relatively uniform. The longitudinal stress is concentrated in the three areas where the slope surface outcrops are more prominent, and the shear stress is concentrated at the bottom because of the accumulation of gravitational forces. In the experimental group, the changes in the three indicators are significantly controlled by discontinuities, indicating that the fissures that cut around the DFN on the model surface are concentrated. From the perspective of the displacement field, compared with that in the control group, the Z-direction displacement in the experimental group significantly increased, and the displacement distribution clearly exhibited nonuniformity, with concentrated displacements in local areas. This finding indicates that the random joint fractures disrupted the continuity of the rock mass, causing the deformation to no longer be uniform, and the surrounding areas of the fractures became weak regions with concentrated displacements. The overall deformation capacity significantly improved. From the stress field perspective, the ZZ stress and the maximum shear stress in the experimental group significantly increased, and the stress concentration areas were highly correlated with the distribution of joint fractures. This occurred because the random joint fractures changed the stress transmission path, and the fracture surfaces were prone to stress concentration, whereas the interior of the fractures experienced stress release, resulting in a "scattered concentration and overall disorder" characteristic of the stress field. These results demonstrate that the mechanical behavior and stability of rock slopes are significantly controlled by the geometry and distribution of discontinuities. Therefore, in practical engineering applications, a detailed investigation of discontinuity networks is essential.

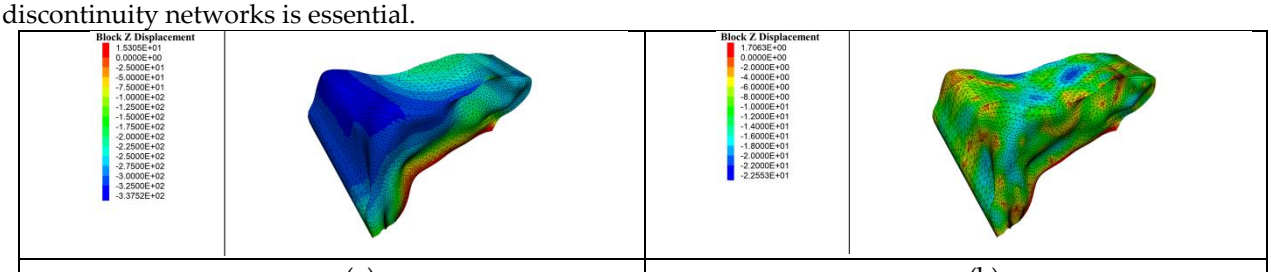

(a) (b)

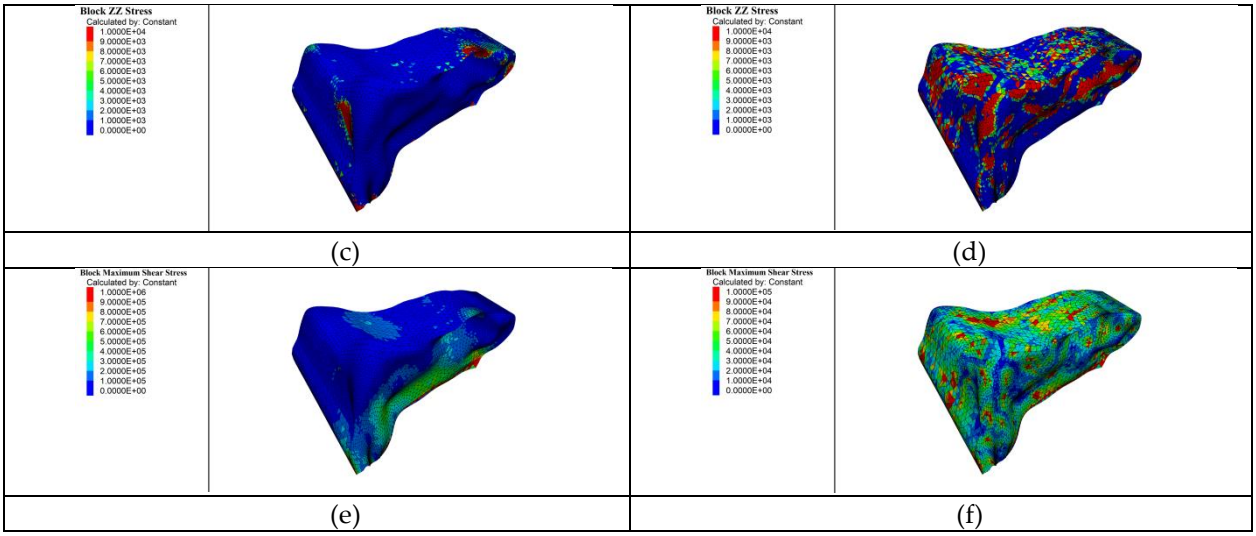

Fig. 15. Results of the simulation: left: control group. right: experimental group. (a)(b) Longitudinal displacement; (c)(d) longitudinal stress; (e)(f) maximum shear stress.

5 Discussion

5.1 Advantage

This study proposes a DBSCAN dual clustering method guided by a curvature threshold, which avoids the application of DPC to the entire point cloud, greatly improves the processing efficiency, and enables the complete extraction of individual discontinuities. First, curvature-based filtering is applied to remove points near discontinuity intersections, followed by DBSCAN clustering to segment the point cloud into a series of individual discontinuities. Although these segments may not fully represent all discontinuities, they effectively capture the dominant orientation patterns and serve as a compact, representative dataset for the subsequent step. To efficiently identify the discontinuity sets, the normal vectors of the initially extracted discontinuity are used as inputs to the DPC. Compared with applying DPC directly to the entire point cloud, which typically contains more than 100,000 points, the number of these normal vectors is only a few hundred to a few thousand. This substantial reduction in input size significantly improves the computational efficiency of DPC, enabling rapid identification of cluster centers. Once the discontinuity sets are determined on the basis of orientation similarity, DBSCAN clustering is then reapplied to the points within each discontinuity set to refine the segmentation and identify complete individual discontinuities. This hierarchical clustering framework enables accurate discontinuity identification while maintaining computational efficiency. As shown in Tables 6 and 7, the data used in Table 6 are from the study area, with a point cloud count of 439,157, and the data used in Table 7 are from another rocky slope in the same area, with a point cloud count of 745,960. Compared with directly applying DPC to the entire point cloud, the proposed method reduces the computing time from 2235 seconds to 244 seconds and from 6361 seconds to 618 seconds in the distribution of two sample datasets, which indicates a significant improvement in processing efficiency.

Table 6. Comparison between the proposed method and classic DPC methods (439,157)

	Proposed Method	**Classic DPC**
Procedure	Time(s)	Time(s)
Point cloud feature	22.87	22.87
Individual discontinuity recognition	221.39	2211.63

Discontinuity characterization	Total	244	Total	2235
	Orientation	0.09	Orientation	0.11
	Trace Length	5.12	Trace Length	6.24
	Spacing	46.36	Spacing	56.39

Table 7. Comparison between the proposed method and classic DPC (745,960)

	Proposed Method		**Classic DPC**	
Procedure		Time(s)		Time(s)
Point cloud feature		52.36		52.36
Individual discontinuity recognition		565.42		6308.90
	Total	618	Total	6361
Discontinuity characterization	Orientation	0.21	Orientation	0.225
	Trace Length	11.02	Trace Length	12.36
	Spacing	56.45	Spacing	121.32

5.2 Limitation

Although the method proposed in this study has achieved good results in identifying structural planes on high and steep slopes at the Pulang copper mine, several limitations should be noted when applying it:

(1) The primary limitation stems from the survey area's environment. The slopes at the Prang copper mine are densely vegetated, obscuring much of the rock surface. Although the vegetation point clouds were removed through manual prefiltering, structural planes completely covered by vegetation could not be recovered, which may have led to underestimations of the density, connectivity, and trace integrity of the structural planes. The limited effectiveness of unmanned aerial vehicle (UAV) photogrammetry for vegetated areas is a common problem. In the future, combining multispectral or LiDAR technology could partially penetrate vegetation.

(2) The method involves setting multiple key parameters, and their selection is somewhat empirical and subjective. For example, the nearest neighbor number, curvature segmentation threshold, neighborhood radius for DBSCAN, and minimum number of points in PCA were determined through repeated experiments. Although these values are applicable to the data of this study, they may need to be readjusted when applied to other geological scenarios. In particular, DBSCAN parameters are highly sensitive whether the clustering results are "oversegmented" or "undermerged," and there is a lack of universal automatic optimization criteria.

(3) When geometric parameters are extracted, some simplified models are adopted to balance efficiency and complexity. The trace length calculation considers only the distance between the farthest points at both ends of the trace line, ignoring any possible zigzag shape, which may overestimate its actual through length. The spacing calculation assumes that structural planes in the same group are strictly parallel and projected onto the same plane. This introduces errors when there is a certain degree of dispersion in the occurrence of structural planes. Although these simplifications are common in engineering practice, they remain a source of precision loss.

(4) Inherent bias from trace censoring and truncation. The methodology primarily captures discontinuities that are exposed as planar features on the rock surface. A significant limitation is the censoring problem, where trace lengths that extend beyond the boundary of the exposed rock face are cut off, leading to an underestimation of the true trace length. Furthermore, the method is inherently biased towards identifying only the planar portions of discontinuities. Non-planar features, such as curved or irregular fractures, may be oversegmented into multiple smaller planes or misidentified, and thus not accurately represented. This limitation should be clearly acknowledged, as it implies that the derived parameters describe the observable, planar fraction of the fracture network, which may not fully capture the complexity of the subsurface fracture system.

(5) Implications for Discrete Fracture Network (DFN) modeling. The applicability of the extracted parameters for DFN modeling is subject to the limitations described above. While the method successfully identifies the mean orientations of discontinuity sets, it does not directly calculate the K-Fisher dispersion coefficient, a critical input for stochastic DFN generation that describes the variability of orientations within a set. Although the standard deviation of orientation can be used as a proxy, its direct conversion to the K-Fisher coefficient requires careful consideration. Similarly, as noted in point (4), the underestimation of trace length due to censoring can lead to a DFN with shorter, less connected fractures than in reality, potentially resulting in an overly optimistic assessment of rock mass strength and stability. Therefore, while the method provides a robust geometric foundation, users should be aware that the resulting DFN is a simplified model based on observable planar data, and its predictions should be interpreted with these inherent uncertainties in mind.

6 Conclusion

On the basis of the slope stability risk management requirements in the mining area of the Pulang copper mine, this paper proposes a new method that integrates curvature-threshold filtering, DBSCAN clustering, and the DPC algorithm to identify discontinuity sets effectively and extract key geometric parameters.

This method was successfully applied to the complex topographic and geological conditions of the Pulang copper mine, where steep terrain, high vegetation coverage, and inaccessible slopes make traditional survey techniques infeasible. The UAV-derived point cloud provided high-resolution data, which, after preprocessing and dual-stage clustering, allowed for the identification of discontinuity sets and individual discontinuities. Compared with conventional DPC, the proposed framework reduces the computational time by 89%, enabling rapid analysis even with large-scale datasets. The identified discontinuities were validated against manually fitted planes in CloudCompare, with orientation deviations remaining within acceptable limits. The trace length and spacing parameters were also extracted and used to construct a DFN. This DFN was embedded into a slope model constructed from real terrain data and used in discrete element simulations to evaluate slope behavior under self-weight conditions. The results clearly demonstrated that discontinuities significantly influence the stress distribution and deformation.

This case study demonstrates that the proposed method is applicable in real-world high-risk mining scenarios. For high and steep, dangerous slopes that are difficult to survey via traditional methods, this paper has verified the practicability of the integrated workflow of unmanned aerial vehicle photogrammetry + intelligent point cloud processing, providing a safe and efficient alternative solution for rock structure investigations in areas such as mining sites, highway slopes, and hydropower projects. This method is applicable not only to the initial survey but also to the efficient data acquisition and processing capabilities, which are suitable for the verification of geological records during the construction period and the periodic monitoring of slope stability during the operation period. Through regular flights and change detection, the development trend of structural planes or deformation of rock masses can be tracked, providing dynamic data support for safe production in mines and early warning of disasters.

Author Contributions: Conceptualization, L.W.; methodology, X.L.; software, X.L.; validation, Y.W. and B.W.; formal analysis, Y.W.; investigation, X.L. and Z.L.; resources, L.W.; data curation, X.L. and Z.L.; writing—original draft preparation, S.W.; writing—review and editing, X.L. and Z.L.; visualization, J.Y.; supervision, J.Y.; project administration, X.Y.; funding acquisition, L,W. All the authors have read and agreed to the published version of the manuscript.

Funding: This research was funded by the Deep Underground National Science and Technology Major Project of China (Grant No. 2024ZD1001400).

Data availability statement: The data and materials that support the findings of this study are available from the author Xinlong Liu upon reasonable request.

Conflicts of interest: The authors declare that they have no conflicts of interest.

References

[1]. Ma, X., Qi, S., Zhu, W. et al. Identification and characterization of rock discontinuities under complex terrain conditions based on UAV photogrammetry and ANN algorithm. *Bull Eng Geol Environ* **2025**, 84, 170. https://doi.org/10.1007/s10064-025-04193-3

[2]. Migliazza, M., Carriero, M.T., Lingua, A., Pontoglio, E., Scavia, C. Rock Mass Characterization by UAV and Close-Range Photogrammetry: A Multiscale Approach Applied along the Vallone dell'Elva Road. *Geosciences* **2021**, 11, 436. https://doi.org/10.3390/geosciences11110436

[3]. Cai, X., Lü, Q., Zheng, J., Liao, K.-W., & Liu, J. An efficient adaptive approach to automatically identify rock discontinuity parameters using 3D point cloud model from outcrops. *Geological Journal* **2023**, 58(6), 2195–2210. https://doi.org/10.1002/gj.4708

[4]. Li, T., Zhang, W., Lu, C. et al. Exposed Linear Discontinuity Recognition on A High Steep Slope Using UAV Multisource Image Fusion. *Rock Mech Rock Eng* **2025**, 58, 9669–9693. https://doi.org/10.1007/s00603-025-04652-z

[5]. Tang, M., Yang, S., Huang, G., Xie, X., Guo, J., Zhai, J. Automatic Extraction of Rock Discontinuities from the Point Cloud Using Dynamic DBSCAN Algorithm, *Advances in Civil Engineering* **2022**, 7754179, 8 pages,. https://doi.org/10.1155/2022/7754179

[6]. Khanna, R., Dubey, R.K. Comparative assessment of slope stability along road-cuts through rock slope classification systems in Kullu Himalayas. *Bull Eng Geol Environ* **2021**, 80, 993–1017. https://doi.org/10.1007/s10064-020-02021-4

[7]. Muhammad J., Rini A.A., Radzuan S., Mohd N.A.A. An expeditious approach for slope stability assessment using integrated 2D electrical resistivity tomography and unmanned aerial vehicle survey, *Journal of Applied Geophysics* **2022**, Volume 205 , 104778, ISSN 0926-9851, https://doi.org/10.1016/j.jappgeo.2022.104778.

[8]. Loupasakis, C., Tsangaratos, P., Gatsios, T., Eleftheriou, V., Parcharidis, I., Soupios, P. Investigating the Stability of the Hill of the Acropolis of Athens, Greece, Using Fuzzy Logic and Remote Sensing Techniques. *Remote Sens.* **2023**, 15, 1067. https://doi.org/10.3390/rs15041067

[9]. Abellán, A., Oppikofer, T., Jaboyedoff, M., Rosser, N.J., Lim, M. and Lato, M.J. Terrestrial laser scanning of rock slope instabilities. Earth Surf. Process. *Landforms* **2014**, 39: 80-97. https://doi.org/10.1002/esp.3493

[10]. Haneberg, W.C. Using close range terrestrial digital photogrammetry for 3-D rock slope modeling and discontinuity mapping in the United States. *Bull Eng Geol Environ* **2008**, 67, 457–469. https://doi.org/10.1007/s10064-008-0157-y

[11]. Li, M.; Xiu, Z.; Han, J.; Meng, F.; Wang, F.; Ji, H. Characterization and Stability Analysis of Rock Mass Discontinuities in Layered Slopes: A Case Study from Fushun West Open-Pit Mine. *Appl. Sci.* **2024**, 14, 11330. https://doi.org/10.3390/app142311330

[12]. Hartwig, M.E., Santos, G.G.d.S.d. Enhanced discontinuity mapping of rock slopes exhibiting distinct structural frameworks using digital photogrammetry and UAV imagery. *Environ Earth Sci.* **2024**, 83, 624. https://doi.org/10.1007/s12665-024-11939-x

[13]. Chen, N., Hao, Y., Wang, C., & Zheng, J. Semiautomatic identification of discontinuity parameters in rock masses based on Unmanned Aerial Vehicle photography. *Geological Journal* **2024**, 59(9), 2401–2415. https://doi.org/10.1002/gj.4905

[14]. Li, H., Li, X., Li, W., Zhang, S., Zhou, J. Quantitative assessment for the rockfall hazard in a postearthquake high rock slope using terrestrial laser scanning, *Engineering Geology* **2019**, Volume 248, Pages 1-13, ISSN 0013-7952, https://doi.org/10.1016/j.enggeo.2018.11.003.

[15]. Wu, X.; Wang, F.; Wang, M.; Zhang, X.; Wang, Q.; Zhang, S. A New Method for Automatic Extraction and Analysis of Discontinuities Based on TIN on Rock Mass Surfaces. *Remote Sens* **2021**, 13, 2894. https://doi.org/10.3390/rs13152894

[16]. Liu, Y.; Hua, W.; Chen, Q.; Liu, X. Characterization of Complex Rock Mass Discontinuities from LiDAR Point Clouds. *Remote Sens.* **2024**, 16, 3291. https://doi.org/10.3390/rs16173291

[17]. Chen, N., Xiao, A., Li, L. et al. Semiautomatic Identification of Tunnel Discontinuity Based on 3D Laser Scanning. *Geotech Geol Eng* **2024**, 42, 2577–2599. https://doi.org/10.1007/s10706-023-02692-2

[18]. Lu, G., Cao, B., Zhu, X., Lin, Z., Bai, D., Tao, C., Li, Y. Identification of rock mass discontinuity from 3D point clouds using improved fuzzy C-means and convolutional neural network. *Bulletin of Engineering Geology and the Environment* **2024**, 83(5), 159.

[19]. Cao, B., Zhu, X., Lin, Z., Li, Y., Yang, Z., Lu, G. Semiautomatic measurement for rock mass discontinuity orientation, trace and spacing from point clouds. *Measurement* **2025**, 246, 116688.

[20]. Yalcin, I., Can, R., Gokceoglu, C., & Kocaman, S. A Novel Rock Mass Discontinuity Detection Approach with CNNs and Multi-View Image Augmentation. *ISPRS International Journal of Geo-Information* **2024**, 13(6), 185. https://doi.org/10.3390/ijgi13060185

[21]. S. Palazzo et al. Domain Adaptation for Outdoor Robot Traversability Estimation from RGB data with Safety-Preserving Loss, *International Conference on Intelligent Robots and Systems* **2020**, pp. 10014-10021, doi: 10.1109/IROS45743.2020.9341044.

[22]. Kang, J., Fu, X., Sheng, Q. et al. Semiautomatic identification of rock discontinuity orientation based on 3D point clouds and its engineering application. *Bull Eng Geol Environ* **2024**, 83, 172. https://doi.org/10.1007/s10064-024-03681-2

[23]. Ma, L., Zuo, C., Qiu, H. et al. A Multilevel Classification Strategy for the Identification of Discontinuities from 3D Point Clouds of Complicated Rock Surfaces. *Rock Mech Rock Eng* **2024**, 57, 10611–10630. https://doi.org/10.1007/s00603-024-04109-9

[24]. Kong, D., Wu, F. Charalampos Saroglou, Automatic identification and characterization of discontinuities in rock masses from 3D point clouds, *Engineering Geology* **2020**, Volume 265, 105442, ISSN 0013-7952, https://doi.org/10.1016/j.enggeo.2019.105442.

[25]. Zhu, J., Xia, Y., Wang, B., Yang, Z., Yang, K. Research on the Identification of Rock Mass Structural Planes and Extraction of Dominant Orientations Based on 3D Point Cloud. *Appl. Sci.* **2024**, 14, 9985. https://doi.org/10.3390/app14219985

[26]. Ozturk, H, S ., Kocaman, S., Gokceoglu, C. A low-cost approach for determination of discontinuity orientation using smartphone images and application to a part of Ihlara Valley (Central Turkey), *Engineering Geology* **2019**, Pages 63-75, ISSN 0013-7952, https://doi.org/10.1016/j.enggeo.2019.04.011.

[27]. Kang, J., Fu, X., Sheng, Q., Ge, Y., Chen, J., Wang, H. Semiautomatic identification of rock discontinuity orientation based on 3D point clouds and its engineering application. *Bulletin of Engineering Geology and the Environment* **2024**, 83(5), 1-18.

[28]. Zang, W., Liu, X., Ma, L., Sun, M., Che, J., Zhao, Y., Wang, Y., Wang, D., Liu, X. DPC-MFP: An adaptive density peaks clustering algorithm with multiple feature points, *Neurocomputing* **2025**, Volume 618, 129060, ISSN 0925-2312, https://doi.org/10.1016/j.neucom.2024.129060.

[29]. Cao, B., Zhu, X., Lin, Z., Li, Y., Yang, Z., Lu, G. Semiautomatic measurement for rock mass discontinuity orientation, trace and spacing from point clouds, *Measurement* **2025**, Volume 246, 116688, ISSN 0263-2241, https://doi.org/10.1016/j.measurement.2025.116688.

[30]. Gu, D., Huang, D. A complex rock topple-rock slide failure of an anaclinal rock slope in the Wu Gorge, Yangtze River, China, *Engineering Geology* **2016**, Volume 208, Pages 165-180, ISSN 0013-7952, https://doi.org/10.1016/j.enggeo.2016.04.037.